Midrapidity hyperon production in pp and pA collisions from low to LHC energies

G.H. Arakelyan[1], C. Merino[2], and Yu.M. Shabelski[3]

[1]A.Alikhanyan National Scientific Laboratory
(Yerevan Physics Institut)
Yerevan, 0036, Armenia
E-mail: argev@mail.yerphi.am

[2]Departamento de Física de Partículas, Facultade de Física
and Instituto Galego de Física de Altas Enerxías (IGFAE)
Universidade de Santiago de Compostela
Santiago de Compostela 15782
Galiza-Spain
E-mail: merino@fpaxp1.usc.es

[3]Petersburg Nuclear Physics Institute
NCR Kurchatov Institute
Gatchina, St.Petersburg 188350, Russia
E-mail: shabelsk@thd.pnpi.spb.ru

Abstract

The experimental data on p, Λ, Ξ^-, Ω^--baryons and the corresponding antibaryons spectra obtained by different collaborations are compared with the results of the calculations performed into the frame of the Quark-Gluon String Model. The contribution of String Junction diffusion and the inelastic screening corrections are accounted for in the theoretical calculations. The predictions of the Quark-Gluon String Model both for pp and pA collisions are extended up to the LHC energies.

PACS. 25.75.Dw Particle and resonance production

1 Introduction

The study of hadron production has a long history in high-energy particle and nuclear physics, as well as in cosmic-ray physics. The absolute yields and the transverse momentum (p_T) spectra of identified hadrons in high-energy hadron-hadron collisions are among the most basic physical observables. They can be used to test the predictions for non-perturbative quantum chromodynamics (QCD) processes like hadronization and soft-parton interactions, and the validity of their corresponding implementation in Monte Carlo (MC) event generators [1, 2, 3].

Among the different available phenomenological models, in this paper we will consider the Quark-Gluon String Model (QGSM) [4, 5], based on the Dual Topological Unitarization, Regge phenomenology, and nonperturbative notions of QCD, and that has been successfully used for the description of multiparticle production processes in hadron-hadron [6, 7, 8, 9, 10] and hadron-nucleus [11, 12, 13, 14, 15] collisions.

In the QGSM high energy interactions are considered as proceeding via the exchange of one or several Pomerons, and all elastic and inelastic processes result from cutting through or between Pomerons [16]. Inclusive spectra of hadrons are related to the corresponding fragmentation functions of quarks and diquarks, which are constructed using the Reggeon counting rules [17].

In the case of interaction with a nuclear target, the Multiple Scattering Theory (Gribov-Glauber Theory) is used, what allows to consider the interaction with nucleus as the superposition of interactions with different numbers of target nucleons [11].

The QGSM gives a reasonable description of a lot of experimental data on baryons and strange hyperons production in hadron-hadron collisions for wide energy range going from fixed target experiments up to LHC [6, 7, 8, 10, 9, 11, 12, 13, 14, 15]. In this paper we extend the model to the study the multistrange hyperon production.

The multistrange baryons, Ξ^- (dss), and Ω^- (sss), are particulary important in high energy particle and nuclear physics, due to their dominant strange quark (s-quark) content. Since the initial-state colliding projectiles contain no strange valence quarks, all particles in the final state with non-zero strangeness quantum number should have been created in the course of the collision. Moreover, the energy of the Large Hadron Collider (LHC) and its high luminosity allow for an abundant production of strange hadrons. These two factors make multi-strange baryons a valuable probe in understanding the particle production mechanisms in high energy collisions.

A remarkable feature of strangeness production is that the production of each additional strange quark featuring in the secondary baryons, i.e., the production rate of secondary $B(qqs)$ over secondary $B(qqq)$, then of $B(qss)$ over $B(qqs)$, and, finally, of $B(qss)$ over $B(sss)$, is affected by one universal strangeness suppression factor, λ_s:

$$\lambda_s = \frac{B(qqs)}{B(qqq)} = \frac{B(qss)}{B(qqs)} = \frac{B(qss)}{B(sss)} \,, \tag{1}$$

together with some simple combinatorics [13, 18, 19].

It will be shown below that λ_s slightly increases with initial energy, the experimental data favoring the value λ_s=0.22 at fixed target eneries ($\sqrt{(s)} \leq 30$ GeV), that becomes λ_s=0.32 at larger RHIC and LHC energies. This energy dependence can be connected to an increase of hardness of the interacton, i.e. to the increase of the secondaries average transverse momenta [20].

Significant differences in the yields of baryons and antibaryons in the central (midrapidity) region are evident at not very high energies. This effect can be naturally explained [8, 9, 10, 21, 22, 23] by the structure of baryons in QGSM, i.e. baryons of three valence quarks together with a specific configuration of the gluon field, called String Junction [24, 25, 26, 27].

At very high energies the contribution of the enhanced Reggeon diagrams becomes important, leading to a new phenomenological effect, the suppression of the inclusive density of secondaries [28] in the central (midrapidity) region.

We present a brief description of the model in Section 2. In Section 3 we show the comparison of our numerical calculations with the existing experimental data on secondary baryons and antibaryons production in pp and pA collisions. Conclusion remarks are given in Section 4.

2 QGSM formalism

2.1 General approach

The QGSM [4, 6, 7] allows one to make quantitative predictions for different features of multiparticle production, in particular, for the inclusive densities of different secondaries, both in the central and in the beam fragmentation regions.

In QGSM, each exchanged Pomeron corresponds to a cylindrical diagram, and thus, when cutting one Pomeron, two showers of secondaries are produced (see Fig. 1 a,b).

The inclusive spectrum of a secondary hadron h is then determined by the convolution of the diquark, valence quark, and sea quark distributions, $u(x,n)$, in the incident particles, with the fragmentation functions, $G^h(z)$, of quarks and diquarks into the secondary hadron h. Here n is the number of cutted Pomerons in the considered diagrams. Both the distributions and the fragmentation functions are constructed using the Reggeon counting rules [17].

In particular, in the case of $n > 1$, i.e. in the case of multipomeron exchange, the distributions of valence quarks and diquarks are softened due to the appearance of a sea quark contribution.

The details of the model are presented in [4, 6, 7, 10]. The average number of

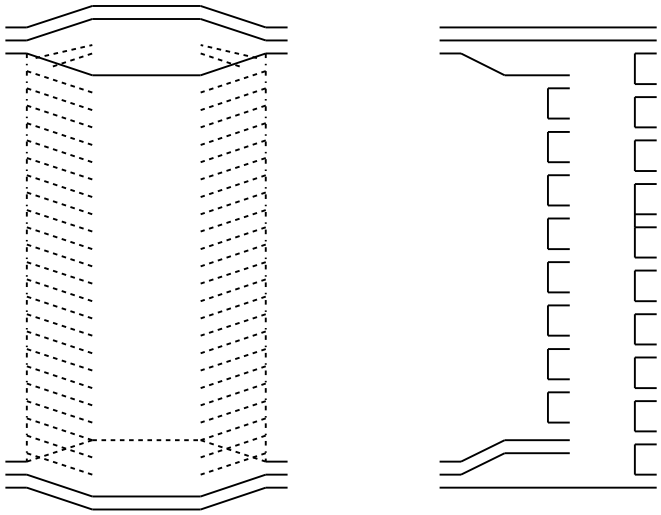

Figure 1: (a) Cylindrical diagram representing a Pomeron exchange within the DTU classification (quarks are shown by solid lines); (b) One cut of the cylindrical diagram corresponding to the single-Pomeron exchange contribution in inelastic pp scattering.

exchanged Pomerons $\langle n \rangle_{pp}$ slowly increases with the energy. The values of the Pomeron parameters have been taken from [7].

For a nucleon target, the inclusive rapidity, y, or Feynman-x, x_F, spectrum of a secondary hadron h has the form [4]:

$$\frac{dn}{dy} = \frac{x_E}{\sigma_{inel}} \cdot \frac{d\sigma}{dx_F} = \sum_{n=1}^{\infty} w_n \cdot \phi_n^h(x) \ , \tag{2}$$

where the functions $\phi_n^h(x)$ determine the contribution of diagrams with n cut Pomerons, w_n [4] is the relative weight of this diagram. Here we neglect the numerically small contribution of diffraction dissociation processes.

In the case of pp collisions:

$$\phi_n^h(x) = f_{qq}^h(x_+,n)\cdot f_q^h(x_-,n)+f_q^h(x_+,n)\cdot f_{qq}^h(x_-,n)+2(n-1)\cdot f_s^h(x_+,n)\cdot f_s^h(x_-,n) \ , \tag{3}$$

$$x_\pm = \frac{1}{2}[\sqrt{4m_T^2/s + x^2} \pm x] \ , \tag{4}$$

where f_{qq}, f_q, and f_s correspond to the contributions of diquarks, valence quarks, and sea quarks, respectively.

These contributions are determined by the convolution of the diquark and quark distributions with the fragmentation functions, e.g.,

$$f_q^h(x_+,n) = \int_{x_+}^1 u_q(x_1,n) \cdot G_q^h(x_+/x_1)dx_1 \ . \tag{5}$$

2.2 String Junction contribution

In the string models, baryons are considered as configurations consisting of three connected strings (related to three valence quarks), called String Junction (SJ) [24, 25, 26, 27], this picture leading to some quite general phenomenological predictions.

The production of a baryon-antibaryon pair in the central region usually occurs via SJ-$\overline{SJ}$ pair production (SJ has upper color indices, whereas anti-SJ ($\overline{SJ}$) has lower indices), which then combines with sea quarks and sea antiquarks into a $B\overline{B}$ pair [26], as it is shown in Fig. 2a.

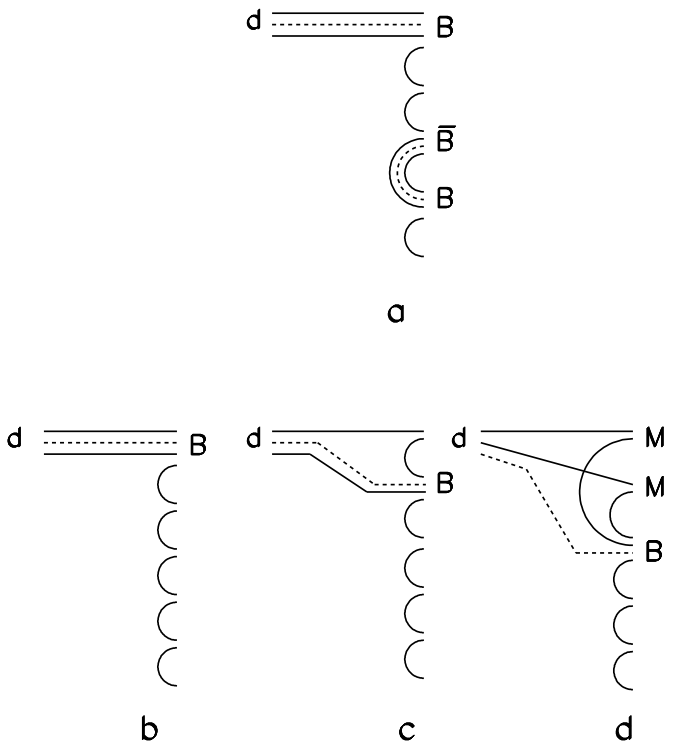

Figure 2: QGSM diagrams describing secondary baryon production: (a) usual $B\overline{B}$ central production with production of new SF pair; (b) initial SF together with two valence quarks and one sea quark; (c) initial SF together with one valence quark and two sea quarks; (d) initial SF together with three sea quarks.

In the case of central production of baryon−antibaryon pairs (Fig. 2a) the fragmentation functions of any quarks and diquarks into antibaryons are proportional to

$$G(z) = a_{\overline{B}} \cdot (1 - Z)^{\beta_{\overline{B}}}, \tag{6}$$

where parameters $a_{\overline{B}}$ and $\beta_{\overline{B}}$ take different values for different antibaryon states. The parameter $\beta_{\overline{B}}$ was described in [10, 11, 13, 29]. In the central region, $z \to 0$, the values of the parameter $a_{\overline{B}}$ in the fragmentation functions of Eq. 5 for $\overline{p}$, $\overline{\Lambda}$, $\overline{\Xi}$, and $\overline{\Omega}$

productions are connected by the following relation [13]:

$$a_{\overline{p}} : a_{\overline{\Lambda}} : a_{\overline{\Xi}} : a_{\overline{\Omega}} = 1 : \sqrt{(5/2)\cdot\lambda_s} : \sqrt{(3/4)\cdot\lambda_s^2} : \sqrt{(1/4)\cdot\lambda_s^3} \ , \tag{7}$$

where λ_s is the strangeness suppression factor (see Introduction), and the numerical factors $\sqrt{5/2}$, $\sqrt{3/4}$, and $\sqrt{1/4}$ are determined by quark combinatorics [10, 18, 19]. The value of the parameter $a_{\overline{p}}$ for $\overline{p}$ production was determined by comparison with the experimental data on antiproton production in pp collisions at different energies to be [11, 13, 29]

$$a_{\overline{p}} = 0.18. \tag{8}$$

The comparatively large value for $\overline{\Lambda}$ production comes from the fact that many strange hyperon resonances (e.g. $\Sigma^*(1385)$) decay into Λ and not into Σ.

By using the relations between $a_{\overline{p}}$, $a_{\overline{\Lambda}}$, $a_{\overline{\Xi}}$ and $a_{\overline{\Omega}}$ in Eq. (7), that derive from simple quark combinatorics [10, 18, 19], we can calculate the $a_{\overline{B}}$ constants in Eq. (6) corresponding to the central production of any strange and multistrange antibaryon in the diagrams describing the central $B\overline{B}$ pair production (see Fig. 2a).

However, in the processes with incident baryons another possibility exists to produce a secondary baryon in the central region, called SJ diffusion (see figs. 2b,c,d).

To obtain the net baryon charge, and according to ref. [10], we consider three different possibilities. The first one is the fragmentation of the diquark giving rise to a leading baryon (Fig. 2b). A second possibility is to produce a leading meson in the first break-up of the string and a baryon in a subsequent break-up [17] (Fig. 2c). In these two first cases the baryon number transfer is possible only along short distances in rapidity. In the third case, shown in Fig. 2d, both initial valence quarks recombine with sea antiquarks into mesons, M, while a secondary baryon is formed by the SJ together with three sea quarks [9, 10].

The fragmentation functions for the secondary baryon B production corresponding to the three processes shown in Fig. 2b, 2c, and 2d can be written as follows (see [10] for more details):

$$G^B_{qq}(z) = a_p \cdot v^B_{qq} \cdot z^{2.5} \ , \tag{9}$$

$$G^B_{qs}(z) = a_p \cdot v^B_{qs} \cdot z^2 \cdot (1-z) \ , \tag{10}$$

$$G^B_{ss}(z) = a_p \cdot \varepsilon \cdot v^B_{ss} \cdot z^{1-\alpha_{SJ}} \cdot (1-z)^2 \ , \tag{11}$$

where

$$a_p = 1.33 \tag{12}$$

is the normalization parameter, obtained earlier from the description of proton spectra in pp collisions [11, 13, 29], and v^B_{qq}, v^B_{qs}, v^B_{ss} are the relative probabilities for different baryons production that can be found by simple quark combinatorics [18, 19] (see Table 1), and the factor ε accounts for the small probability of the process shown in Fig. 2d to occur with respect to the processes in Figs. 2b,c.

B	p	n	$\Lambda+\Sigma^0$	Ξ^0	Ξ^-	Ω^-
v_0	$4L^3$	$4L^3$	$7.5L^2S$	$3LS^2$	$3LS^2$	S^3
v_u	$3L^2$	L^2	$(5/2)LS$	S^2	-	-
v_d	L^2	$3L^2$	$(5/2)LS$	-	S^2	-
v_s	-	-	$(5/2)L^2$	$2LS$	$2LS$	S^3
v_{uu}	$2L$	-	$(1/4)S$	-	-	-
v_{ud}	L	L	S	-	-	-
v_{dd}	-	$2L$	$(1/4)S$	-	-	-
v_{us}	-	-	$(5/4)L$	S	-	-
v_{ds}	-	-	$(5/4)L$	-	S	-
v_{ss}	-	-	-	L	L	S

Table 1: The quark combinatorics providing the values of the parameter v_i^B in eqs. (8−10). Here $S/L=\lambda_s$ and $2L+S=1$.

The probabilities v_{qq}^B, v_{qs}^B, v_{ss}^B depend on the vaule of the strangeness suppression factor λ_s. In [10, 13] we used λ_s=0.32. In the present paper we show that $\lambda_s=0.22$ is in a better agreement with the main sample of the data at intermediate energies (see section 3).

The fraction z of the incident baryon energy carried by the secondary baryon decreases from Fig. 2b to Fig. 2d. Only the processes in Fig. 2d can contribute to the inclusive spectra in the central region at high energies if the value of the intercept of the SJ exchanged Regge-trajectory, α_{SJ}, is large enough. The analysis in [23] gives a value of $\alpha_{SJ}=0.5\pm0.1$, that is in agreement with the ALICE Collaboration result, $\alpha_{SJ}\sim0.5$ [30]. In the present calculations we use [23]:

$$\alpha_{SJ}\,=\,0.5\;\;\text{and}\;\varepsilon\,=\,0.0757\,. \tag{13}$$

2.3 Interaction with nuclei at high energies and inelastic screening effects

In the calculation of the inclusive spectra of secondaries produced in pA collisions we should consider the possibility of one or several Pomeron cuts in each of the ν blobs of proton-nucleon inelastic interactions. For example, in Fig. 3 it is shown one of the diagrams contributing to the inelastic interaction of a beam proton with two target nucleons. In the blob of the proton-nucleon1 interaction one Pomeron is cut, while in the blob of the proton-nucleon2 interaction two Pomerons are cut.

The contribution of the diagram in Fig. 3 to the inclusive spectrum is:

$$\begin{aligned}\frac{dn}{dy}\;=\;\frac{x_E}{\sigma_{prod}^{pA}}\cdot\frac{d\sigma}{dx_F}\;&=\;2\cdot W_{pA}(2)\cdot w_1^{pN_1}\cdot w_2^{pN_2}\cdot\Big\{f_{qq}^h(x_+,3)\cdot f_q^h(x_-,1)\,+\\&+\;f_q^h(x_+,3)\cdot f_{qq}^h(x_-,1)+f_s^h(x_+,3)\cdot[f_{qq}^h(x_-,2)+f_q^h(x_-,2)+\\&+\;2\cdot f_s^h(x_-,2)]\,\}\;,\end{aligned} \tag{14}$$

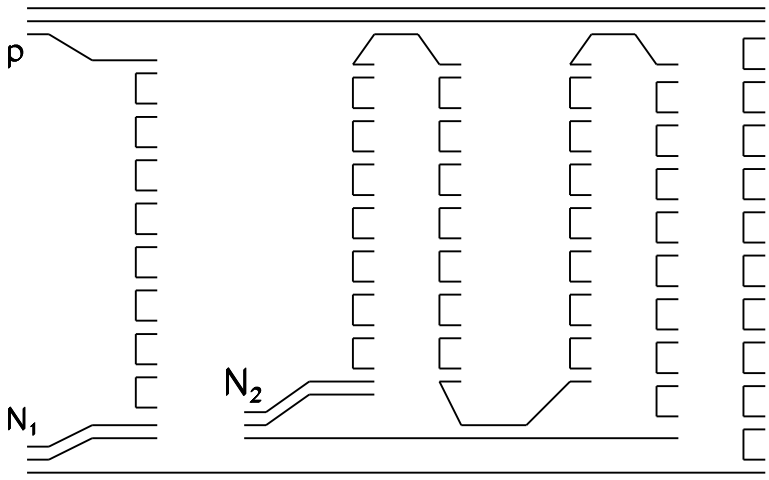

Figure 3: One of the diagrams for the inelastic interaction of one incident proton with two target nucleons N_1 and N_2 in a pA collision.

where $W_{pA}(2)$ is the probability of interaction with namely two target nucleons.

It is essential to take into account all diagrams with every possible Pomeron configuration and its corresponding permutations. The diquark and quark distributions and the fragmentation functions are the same as in the case of pN interaction.

The total number of exchanged Pomerons becomes as large as

$$\langle n\rangle_{pA} \sim \langle \nu\rangle_{pA} \cdot \langle n\rangle_{pN} \ , \tag{15}$$

where $\langle \nu\rangle_{pA}$ is the average number of inelastic collisions inside the nucleus (about 4 for heavy nuclei at fixed target energies).

The process shown in Fig. 3 satisfies [31, 32, 33, 34] the condition that the absorptive parts of the hadron-nucleus amplitude are determined by the combination of the absorptive parts of the hadron-nucleon amplitudes.

The QGSM assumption of the superposition picture of hadron-nucleus interactions gives a reasonable description [9, 11, 35] of the inclusive spectra of different secondaries produced at energies $\sqrt{s_{NN}} = 14{-}30$ GeV.

At RHIC energies the situation drastically changes. The spectra of secondaries produced in pp collisions are described rather well [9], but the RHIC experimental data for $Au{+}Au$ collisions [36, 37] give clear evidence of the inclusive density suppression effects which reduce by a factor $\sim$0.5 the midrapidity inclusive density, when compared to the predictions based on the superposition picture [38, 39]. This reduction can be explained by the inelastic screening corrections connected to multipomeron interactions [28] (see Fig. 4).

At energies $\sqrt{s_{NN}} \leq 30{-}40$ GeV, the inelastic processes are determined by the production of one (Fig. 4a) or several (Fig. 4c) multiperipheral ladders, and the corre-

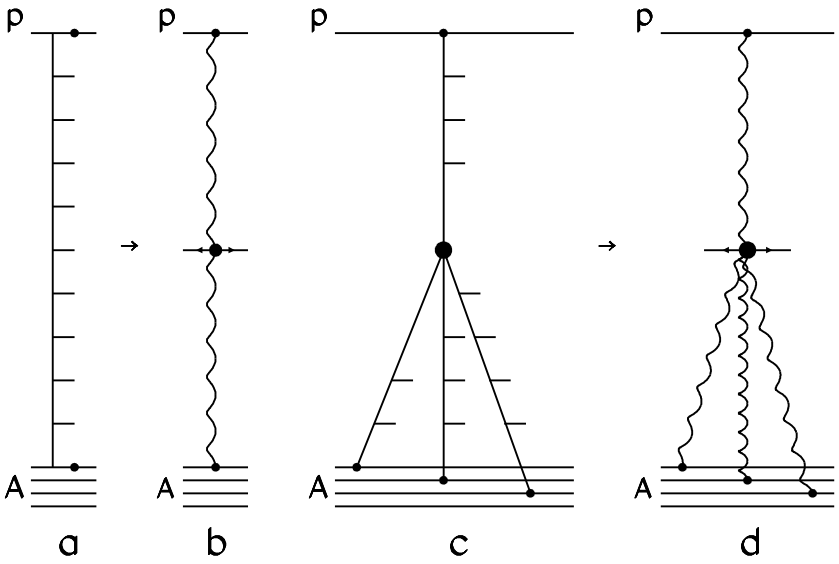

Figure 4: (a) Multiperipheral ladder corresponding to the inclusive cross section of diagram (b), and (c) fusion of several ladders corresponding to the inclusive cross section of diagram (d).

sponding inclusive cross sections are described by the diagrams of figs. 4b and 4d.

In accordance with the Parton Model [40, 41], the fusion of multiperipheral ladders shown in Fig. 4c becomes more and more important with the increase of the energy, resulting in the reduction of the inclusive density of secondaries. Such processes correspond to the enhancement Reggeon diagrams of the type of Fig. 4d, and to even more complicate ones. All these diagrams are proportional to the squared longitudinal form factor of nucleus A [28]. On the contrary, the contribution of such diagrams becomes negligible when the energy decreases, and they are also negligible for pp collisions up to LHC energies.

In any case, all quantitative estimations of the importance of the contribution of the enhanced diagrams are model dependent, since the numerical weight of the contribution of the multipomeron diagrams is rather unclear due to the many unknown vertices in these diagrams. In some models the number of unknown parameters can be reduced, and, as an example, in reference [28] the Schwimmer model [42] was used for the numerical estimations.

Another possibility to weight the contribution of the diagrams with Pomeron interaction comes [43, 44, 45, 46, 47] from Percolation Theory. The percolation approach and its previous version, the String Fusion Model [48, 49, 50], predicted the multiplicity suppression seen at RHIC energies, long before any RHIC data were measured.

In order to account for the percolation (inelastic screening) effects in the QGSM, it is technically more simple [22] to consider a maximal number of Pomerons n_{max} emitted by one nucleon in the central region that can be cut. These cut Pomerons lead to the different final states. Then, the contributions of all diagrams with $n \leq n_{max}$ are

accounted for as at lower energies. The larger number of Pomerons $n > n_{max}$ can also be emitted obeying the unitarity constraint, but due to the fusion in the final state (at the quark-gluon string stage), the cut of $n > n_{max}$ Pomerons results in the same final state as the cut of n_{max} Pomerons.

By doing this, all model calculations become very similar to those in the percolation approach. The QGSM fragmentation formalism allows one to calculate the integrated over p_T spectra of different secondaries as functions of the rapidity and x_F.

In this frame, we obtain a reasonable agreement with the experimental data on the inclusive spectra of secondaries produced in $d + Au$ collisions at RHIC energy [22] with a value $n_{max} = 13$, and in $p + Pb$ collisions at LHC energy [14] with the value $n_{max} = 23$. It has been shown in [51] that the number of strings that can be used for the secondary production should increase with the initial energy.

3 Numerical results

3.1 The pp collisions

The existing experimental data for the integrated over the whole range of p_T energy dependence of p, $\overline{p}$, Λ, $\overline{\Lambda}$, and Ξ^-, $\overline{\Xi}^+$ hyperons production density $dn/dy(\mid y \mid \leq 0.5)$ in pp collisions, from fixed target to LHC energies [52, 53, 54, 55, 56, 57, 58, 59, 60, 61] are compared with the results of the QGSM calculations in Table 2 and in Fig. 5.

The QGSM calculation for secondary p and $\overline{p}$ production in pp collisions performed with the same values of the parameters $a_{\overline{p}}$=0.18 (see Eq. 7) and a_p=1.33 (see Eq. 11) used in our previous papers [11, 29], are in reasonable agreement with the experimental data [54, 62, 63, 64, 65, 66, 67].

For all baryons (p, Λ, Ξ, Ω) and for their corresponding antibaryons, the calculated values for dn/dy($\mid y \mid \leq 0.5$) are shown in Fig. 5 by full curves, and for antibaryons by dashed curves. The theoretical curves and the data on p and $\overline{p}$ production in Fig. 5 are shown as multiplied by a factor 10.

The data on Λ and $\overline{\Lambda}$ [53, 52] productions are reasonably described at the lower energies with the value λ_s=0.22, that should be increased up to λ_s=0.32 at $\sqrt{s} \geq$60 GeV. This increase of the value of λ_s can be connected to the increase in the hardness of the interaction, since then the non-zero value of the s-quark mass becomes not so significant. Possibly, the same effect also leads to the increase of average p_T [21]. At intermediate energies the hardness of the interaction is relatively small and the production of the s-quark, with a mass $m_s \sim 0.3GeV$, is seriously suppressed. At higher enetgies, the hardness of the interaction increases and the effect of the finite s-quark mass becomes not so important, what is refleted by the effective increase of the value of the λ_s parameter. At extremely high energies, as the hardness of the interaction is

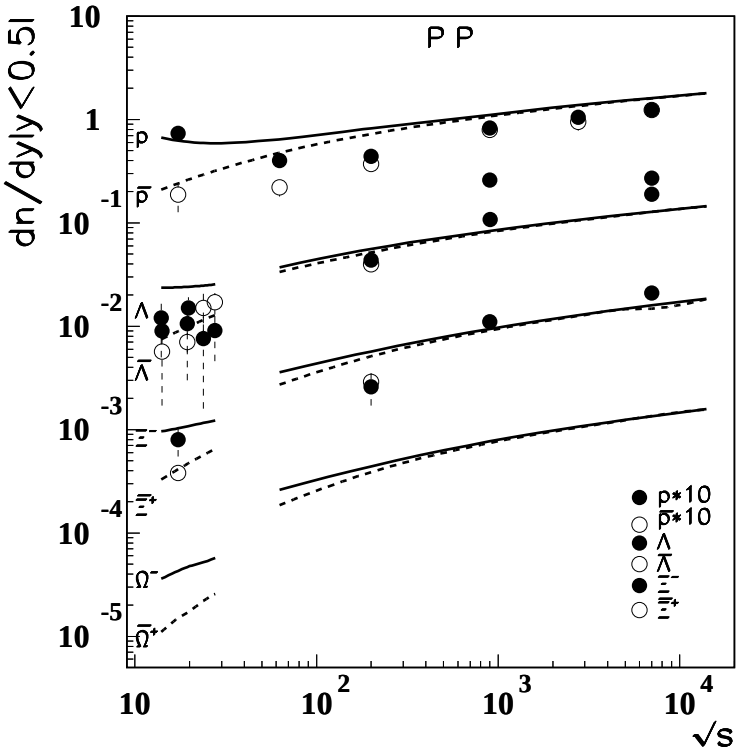

Figure 5: The energy dependence of baryon and antibaryon production inclusive densities $dn/dy(|\ \ y\ | \leq 0.5)$ in the midrapidity region in pp collisions (baryons are shown by closed points and full curves, and antibaryons by open points and dashed curves).

much larger, we expect $\lambda_s \to 1$.

The yields of Ξ^- and $\overline{\Xi}^+$ produced at 158 GeV/c [54] and at LHC energies of 0.9 and 7 Tev [53] are well reproduced by correspondingly using the same values of λ_s=0.22 and λ_s=0.32.

In Fig. 5 we also present our prediction for Ω^- and $\overline{\Omega}^+$ hyperon production.

We do not include in our analysis the ALICE Collaboration data for Ξ^-, $\overline{\Xi}^+$, Ω^- and $\overline{\Omega}^+$ hyperons production [69] at 7 TeV for the reason that these data were measured at transverse momenta $p_T > 0.6$ GeV/c, and therefore they can not be compared to integrated over the whole range of p_T rapidity distributions.

$\sqrt{s}$ (GeV)	Reaction	QGSM	Experiment dn/dy ($\mid y \mid \leq 0.5$)
17.29	$p + p \to p$	0.0605	0.0736 ± 0.015 [68]
	$p + p \to \overline{p}$	0.024	0.054 ± 0.0014 [68]
27.45	$p + p \to p$	0.0576	0.0736 ± 0.015 [62]
	$p + p \to \overline{p}$	0.032	0.01869 ± 0.001 [62]
62.4	$p + p \to p$	0.064	0.040 ± 0.003 [63]
	$p + p \to \overline{p}$	0.0477	0.022 ± 0.002 [63]
200.	$p + p \to p$	0.0454	0.044 ± 0.004 [63]
	$p + p \to \overline{p}$	0.0392	0.037 ± 0.003 [63]
900.	$p + p \to p$	0.111	0.106 ± 0.005 [65]
	$p + p \to p$	0.111	0.083 ± 0.006 [66]
	$p + p \to \overline{p}$	0.107	0.079 ± 0.005 [66]
	$p + p \to \overline{p}$	0.107	0.104 ± 0.003 [65]
2760.	$p + p \to p$	0.138	0.124 ± 0.003 [65]
	$p + p \to \overline{p}$	0.135	0.1235 ± 0.0035 [65]
7000.	$p + p \to p$	0.161	0.15 ± 0.003 [65]
		0.161	0.124 ± 0.009 [67]
	$p + p \to \overline{p}$	0.160	0.147 ± 0.0035 [65]
		0.160	0.123 ± 0.01 [67]
17.29	$p + p \to \Lambda$	0.0219	0.017 ± 0.0004 [54]
	$p + p \to \overline{\Lambda}$	0.0065	0.0057 ± 0.0002 [54]
23.79	$p + p \to \Lambda$	0.0227	0.0132 ± 0.003 [57]
	$p + p \to \overline{\Lambda}$	0.0105	0.010 ± 0.003 [57]
27.45	$p + p \to \Lambda$	0.0233	0.0091 ± 0.0015 [60]
	$p + p \to \overline{\Lambda}$	0.0116	0.017 ± 0.003 [60]
200.	$p + p \to \Lambda$	0.0454	$0.0436 \pm 0.0008 \pm 0.004$ [61]
	$p + p \to \overline{\Lambda}$	0.0392	$0.0398 \pm 0.0008 \pm 0.0037$ [61]
900.	$p + p \to \Lambda$	0.0659	0.26 ± 0.01 [52]
7000.	$p + p \to \Lambda$	0.0987	0.27 ± 0.01 [52]
900.	$p + p \to \Lambda$	0.0659	$0.108 \pm 0.001 \pm 0.012$ [53]
7000.	$p + p \to \Lambda$	0.0987	$0.189 \pm 0.001 \pm 0.022$ [53]
17.29	$p + p \to \Xi^-$	0.000839	0.000799 ± 0.000095 [54]
	$p + p \to \overline{\Xi}^+$	0.000236	0.000381 ± 0.000057 [54]
200.	$p + p \to \Xi^-$	0.00542	$0.0026 \pm 0.0002 \pm 0.0009$ [61]
	$p + p \to \overline{\Xi}^+$	0.00487	$0.0029 \pm 0.0003 \pm 0.006$ [61]
900.	$p + p \to \Xi^-$	0.00942	$0.011 \pm 0.001 \pm 0.001$ [53]
7000.	$P + P \to \Xi^-$	0.0159	$0.021 \pm 0.001 \pm 0.003$ [53]
	$P + P \to \Xi^-$	0.0159	$0.008 \pm 0.001 \pm 0.007$ [69]
	$p + p \to \overline{\Xi}^+$	0.0158	$0.0078 \pm 0.001 \pm 0.007$ [69]
200.	$p + p \to \Omega^- + \overline{\Omega^+}$	0.0000634	$0.00034 \pm 0.00016 \pm 0.0005$ [61]
7000.	$p + p \to \Omega^-$	0.00132	$0.00067 \pm 0.00003 \pm 0.00008$ [69]
	$p + p \to \overline{\Omega}^+$	0.00134	$0.00068 \pm 0.00003 \pm 0.00008$ [69]

Table 2. The experimental data on the inclusive density dn/dy of baryons and antibaryons produced in pp collisions at different energies and their corresponding description by the QGSM.

In Fig. 6 we compare our QGSM calculations with the experimental data on the rapidity dependence of the production cross section $d\sigma/dy$, integrated over the whole p_T range, of proton and antiproton production in pp collisions at two energies, 158 GeV/c [54] and 400 Gev/c [62]. The full curve corresponds to the proton production and the

dashed curve to $\overline{p}$ production, both at 158 GeV/c [54], while the dashed-dotted curve corresponds to p production and the dotted curve to $\overline{p}$ production at 400 GeV/c [62].

On the lower panel of Fig. 6, the Λ and $\overline{\Lambda}$ production cross section $d\sigma/dy$, at 158 GeV/c [54] and at 405 GeV/c [60] in pp collisions are compared with the results of the QGSM calculations. The full curve corresponds to Λ production at 158 GeV/c and the dashed curve to $\overline{\Lambda}$ production at the same energy, while the dashed-dotted curve corresponds to Λ production and the dotted curve to $\overline{\Lambda}$ production, both at 405 Gev/c. All curves for Λ and $\overline{\Lambda}$ production have been obtained with a value of λ_s=0.22. As one can see in Fig. 6, the model calculations agree with the experimetal data.

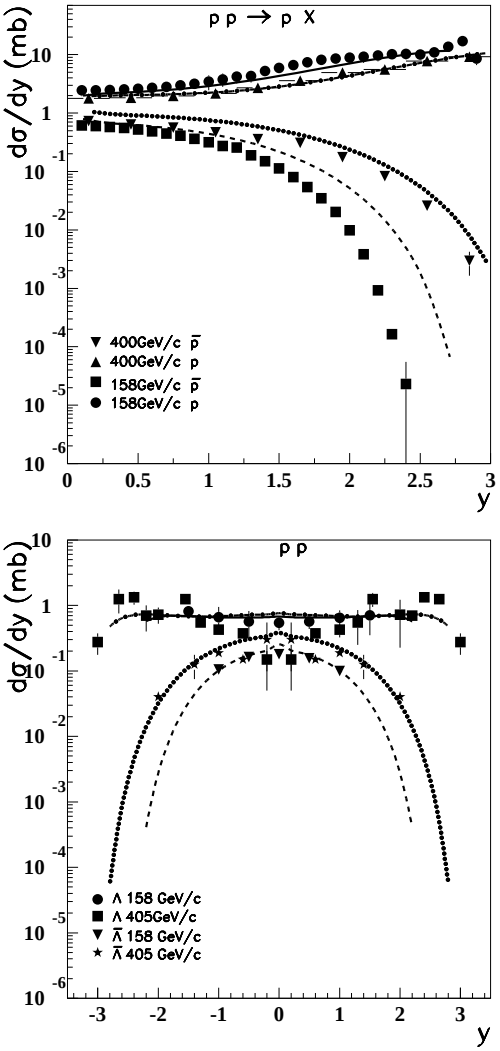

Figure 6: The QGSM results for (upper panel) the rapidity dependence of the production densities dn/dy of p and $\overline{p}$ at 158 GeV/c and 400 GeV/c, and their comparison with the experimental data [54, 62], and for (lower panel) the Λ and $\overline{\Lambda}$ cross sections at 158 GeV/c and 405 GeV/c, and their comparison with the experimental data [54, 60] (see the main text por the description of the different curves).

In Fig. 7 we compare the QGSM calculations for the rapidity dependence of the inclusive cross section $d\sigma/dy$ integrated over the whole p_T range of Ξ^- and $\overline{\Xi}^+$ produced in pp collisions at 158 GeV/c [54]. Also here, the theoretical curves have been data obtained by using the vaue λ_s=0.22. The full curve corresponds to Ξ^- production and the dashed line to the production of $\overline{\Xi}^+$.

On the upper panel of Fig. 8 we show the data on the inclusive density $(1/n_{ev})dn/dy$ for Λ [52, 53] and Ξ^- [53] hyperons production at both 0.9 and 7 TeV. Here it has to be noticed that the data by ATLAS [52] and CMS [53] collaborations at LHC energies 0.9 and 7 TeV are inconsistent with each other, and, in particular, the ATLAS data show a weak energy dependence, while the CMS data would indicate a significantly stronger energy dependence.

As one can see in Fig. 8, the QGSM calculations are in a satisfactory agreement for the cases of Λ production at 0.9 TeV and for Ξ^- production, both at 0.9 and 7 TeV, and they are below the experimental points for Λ production at 7 TeV.

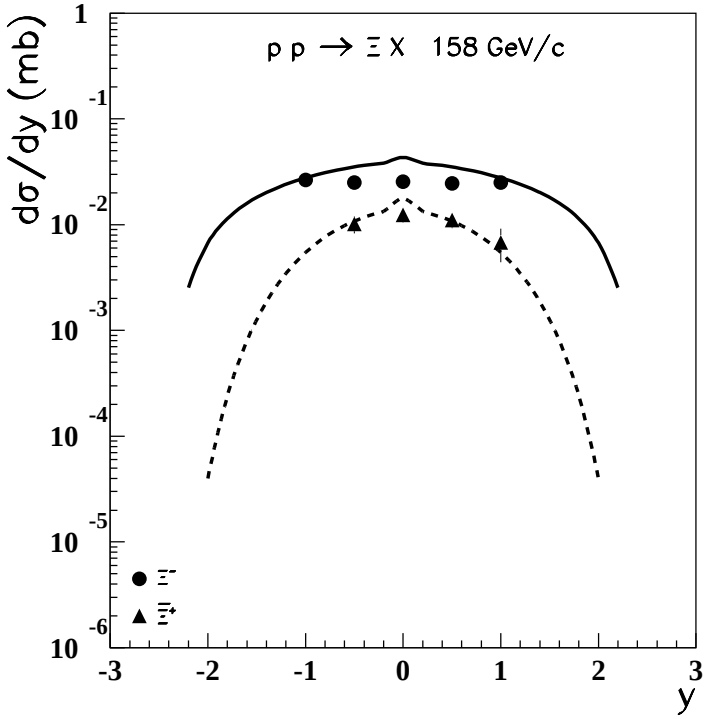

Figure 7: The QGSM results for the rapidity dependence of the inclusive cross section $d\sigma/dy$ of Ξ^- and $\overline{\Xi}^+$ productions in pp collisions at 158 GeV/c, and their comparison with the experimental data [54]. The full curve corresponds to Ξ^- and the dashed curve to $\overline{\Xi}^+$ production.

On the lower panel of Fig. 8 we show the experimental data on rapidity dependence of ratios of Λ/Ξ^- densities at 0.9 and 7 TeV [53] and their comparison with the corresponding QGSM results. The QGSM reasonably reproduces both the values and the rapidity dependences of the Λ/Ξ^- ratios at the two energies.

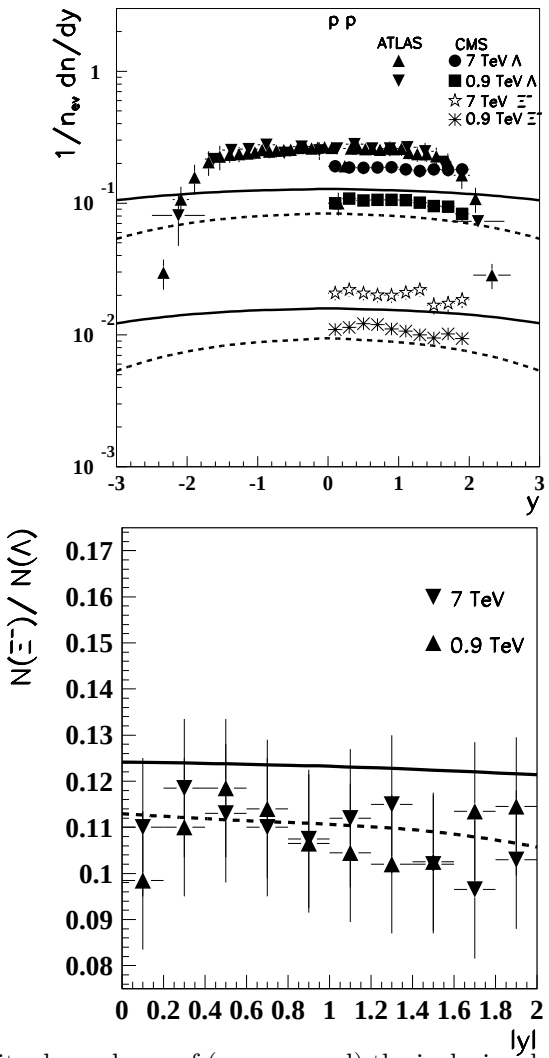

Figure 8: The rapidity dependence of (upper panel) the inclusive density $(1/n_{ev})dn/dy$ of Λ and Ξ^- hyperons production in the midrapidity region for pp collisions at LHC energies [53, 52], and of (lower panel) of the ratio of yields of Λ/Ξ^- hyperons at LHC energies [53] in the midrapidity region for pp collisions [53]. The corresponding QGSM predictions are shown by the full curve ($\sqrt{s}$ = 7 Tev) and by the dashed curve ($\sqrt{s}$ = 0.9 TeV).

3.2 The pA collisions

To perform the calculations corresponding to the case of proton-nucleus interactions we have used the same values of the parameters a_p, $a_{\overline{p}}$, and λ_s as for pp collisions, and we also keep n_{max}= 23 (see subsection 2.3) to account for the inelastic nuclear screening effects.

In Fig. 9 and Table 3 we compare the results of the QGSM calculations for the A-dependences of p, $\overline{p}$, and Λ, $\overline{\Lambda}$, Ξ^-, $\overline{\Xi}^+$, Ω^-, and $\overline{\Omega}^+$ hyperons produced on different nucleus targets with the corresponding experimental data [71, 72, 73, 74, 75]. The QGSM results at 158 GeV/c are presented for all baryons. For Λ and $\overline{\Lambda}$ production two sets of measurements at 158 Gev/c and at 200 GeV/c exist. At 158 GeV/c, the full curves correspond to the production of baryons and the dashed curves to that of

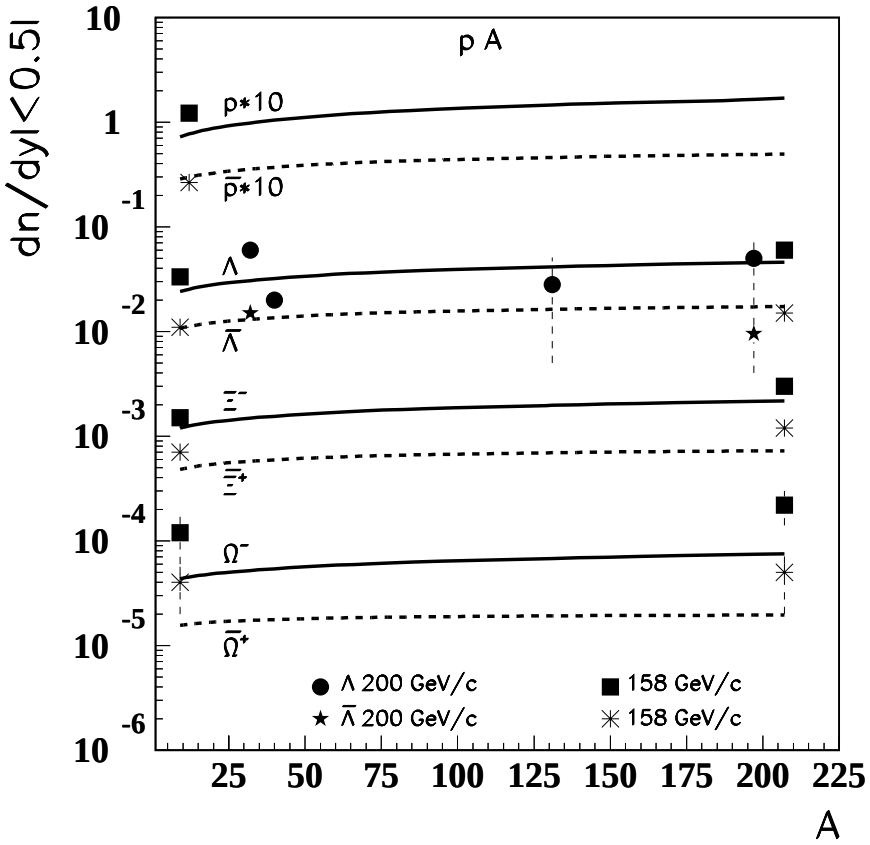

Figure 9: Comparison of experimental data on the A-dependence of midrapidity density dn/dy ($\mid y \mid \leq 0.5$) of p, $\overline{p}$, and Λ, $\overline{\Lambda}$, Ξ^-, $\overline{\Xi}^+$, Ω^-, and $\overline{\Omega}^+$ hyperons produced at 158 Gev/c and 200 GeV/c [71, 73, 74, 75], with the results of corresponding QGSM calculations (see the main text por the description of the different curves).

antibaryons. The curves corresponding to the calculations at 200 GeV/c are very close to those obtained at 158 GeV/c, and then not shown. The QGSM curves are here in a reasonable agreement with the experimental data.

The experimental data on the rapidity density $dn/dy(\mid y \mid \leq 0.5)$ for Λ, $\overline{\Lambda}$, Ξ^-, $\overline{\Xi}^+$, Ω^-, and $\overline{\Omega}^+$ hyperons productions at 158 GeV/c and for p and $\overline{p}$ production at $\sqrt{s}$=5.02 TeV [70] in pPb collisions [71, 73, 74, 75] are presented in Fig. 10, together with the corresponding QGSM predictions from fixed targets up to LHC energies.

Here, as in Fig. 5, the curves for p and $\overline{p}$ production and the CMS Collaboration experimental data on average $(p+\overline{p})/2$ production in p+Pb collisions at $\sqrt{s}$=5.02 TeV [70], have been multiplied by a factor 10 to make them distinct from the Λ and $\overline{\Lambda}$ case.

In Fig. 11 we compare the experimental data on the rapidity dependences of the denstity dn/dy of p and $\overline{p}$ produced in pC collisions measured by the NA49 Collaboration at 158 GeV/c [72], together with the corresponding QGSM calculations. The full curve corresponds to p production and the dashed one to $\overline{p}$ production. The agreement between the QGSM results and the experimental data shown in the figure is rather good.

$\sqrt{s}$ (GeV)	Reaction	QGSM	Experiment dn/dy($\mid y \mid \leq 0.5$)
17.2	p + C $\to p$	0.0720	0.12157 ± 0.005 [72]
	p + C $\to \overline{p}$	0.0285	0.02656 ± 0.0011 [72]
5020.	p + Pb $\to (p+\overline{p})/2$	0.440	0.5 ± 0.05 [70]
17.2	p + Be $\to \Lambda$	0.0241	$0.0334 \pm 0.0005 \pm 0.003$ [71]
	p + Be $\to \overline{\Lambda}$	0.0107	$0.011 \pm 0.0002 \pm 0.001$ [71]
19.42 (200 GeV/c)	p + Ar $\to \Lambda$	0.0320	0.02 ± 0.01 [73]
19.42 (200 GeV/c)	P + Xe $\to \Lambda$	0.0413	0.03 ± 0.015 [73]
19.42 (200 GeV/c)	p + Au $\to \Lambda$	0.0450	0.05 ± 0.01 [74]
19.42 (200 GeV/c)	p + Au $\to \overline{\Lambda}$	0.0193	0.0095 ± 0.01 [74]
19.42 (200 GeV/c)	p + S $\to \Lambda$	0.0306	0.06 ± 0.008 [75]
19.42 (200 GeV/c)	p + S $\to \overline{\Lambda}$	0.0131	0.015 ± 0.003 [75]
17.2	p + Pb $\to \Lambda$	0.0458	$0.060 \pm 0.002 \pm 0.006$ [71]
(m.b.)	p + Pb $\to \overline{\Lambda}$	0.0173	$0.015 \pm 0.001 \pm 0.002$ [71]
17.2	p + Be $\to \Xi^-$	0.0011	$0.0015 \pm 0.0001 \pm 0.0002$ [71]
(m.b.)	p + Be $\to \overline{\Xi}^+$	0.000482	$0.0007 \pm 0.0001 \pm 0.0002$ [71]
17.2	p + Pb $\to \Xi^-$	0.00217	$0.0030 \pm 0.0002 \pm 0.0003$ [71]
(m.b.)	p + Pb $\to \overline{\Xi}^+$	0.000726	$0.0012 \pm 0.0001 \pm 0.0001$ [71]
17.2	p + Be $\to \Omega^-$	0.0000434	$0.00012 \pm 0.00006 \pm 0.00002$ [71]
(m.b.)	p + Be $\to \overline{\Omega}^+$	0.0000155	$0.00004 \pm 0.00002 \pm 0.00001$ [71]
17.2	p + Pb $\to \Omega^-$	0.0000749	$0.00022 \pm 0.00008 \pm 0.00003$ [71]
(m.b.)	p + Pb $\to \overline{\Omega}^+$	0.0000195	$0.00005 \pm 0.00003 \pm 0.00002$ [71]

Table 3. Experimental data for baryons and antibaryons production densities dn/dy ($\mid y \mid \leq 0.5$) in proton-nucleus collisions at different energies, and the corresponding description by the QGSM.

In Fig. 12, the rapidity dependence of the production denstity of Λ hyperon in proton collisions on Ar and Xe nuclei [73] (upper panel) and of Λ and $\overline{\Lambda}$ hyperons produced in proton collisions on S and Au nuclei [74, 75, 76] (lower panel), all at 200 GeV/c, are compared with the results of the corresponding QGSM calculations. The full curve on the upper panel corresponds to Λ production on Ar nucleus and the dash-dotted curve to Λ production on Xe nucleus. On the lower panel, the full curve corresponds to Λ production on Au nucleus, and the dash-dotted curve to Λ production on S nucleus. Also on the lower panel, the dashed curve corresponds to $\overline{\Lambda}$ production on Au nucleus and the dotted curve to $\overline{\Lambda}$ production on S nucleus.

One can generally affirm that QGSM results on the rapidity dependence of the production densities dn/dy of hyperons in pA collisions are in a good agreement with the experimental data at 200 GeV/c, as it is shown in figs. 11 and 12.

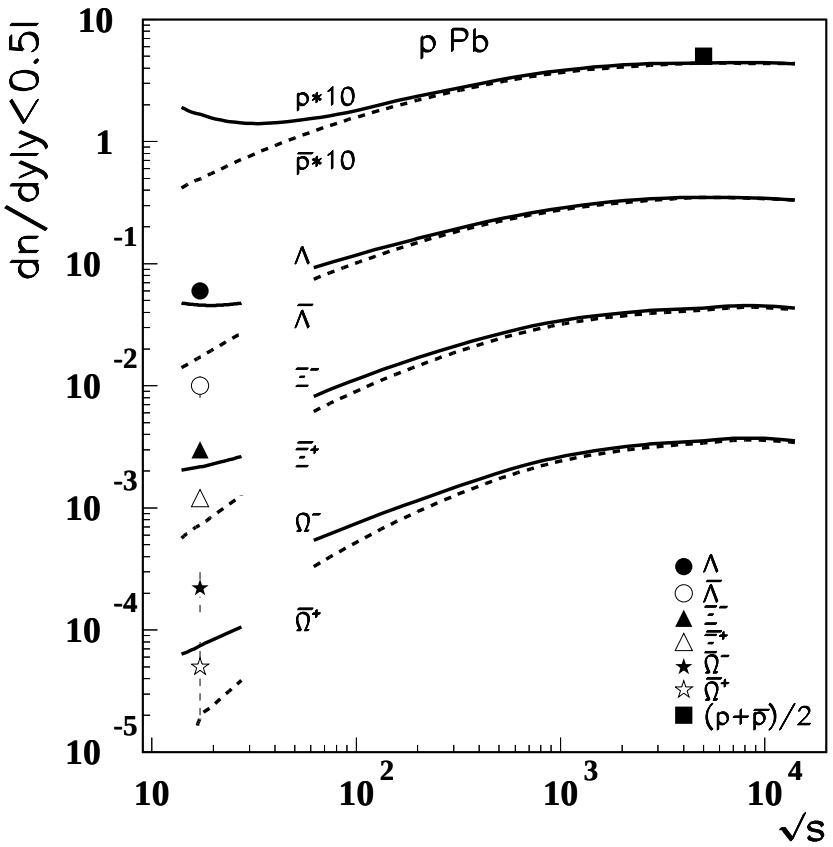

Figure 10: The energy dependence of the baryon production density $dn/dy(\mid y \mid \leq 0.5)$ in the midrapidity region for pPb collisions. The experimental data for average proton production $(p + \overline{p}/2)$ at 5.02 TeV are by the CMS Collaboration [70]. The experimental data on hyperon production were measured by the NA57 Collaboration at 158 GeV/c [71]. The curves are the same as in Fig. 4.

4 Conclusion

The QGSM, based on the Dual Topological Unitarization, Regge phenomenology, and nonperturbative notions of QCD, provides a reasonable description of strange and multistrange hyperons production, as well as of the production of their corresponding antiparticles, both in pp and pA collisions for a wide range of energies, by including into the analysis the contribution of String Junction diffusion and the inelastic screening corrections.

It is important to note that in the QGSM the extension of the calculations of the hyperon (antihyperon) productions from pp collisions to proton-nucleus collisions does not require any additional model parameters. The accuracy of our calculations can be estimated to be on the level of $\sim 15\%$.

The values of the parameters a_p and $a_{\overline{p}}$ in the model obtained from previous calculations at lower energies are now confirmed by the good description of p and $\overline{p}$ production at higher energies. The estimation of the production of all hyperons and antihyperons is governed by the value of only one parameter λ_s, which is the same for every unit of strangeness, but that it depends on energy from the value λ_s=0.22 at fixed target

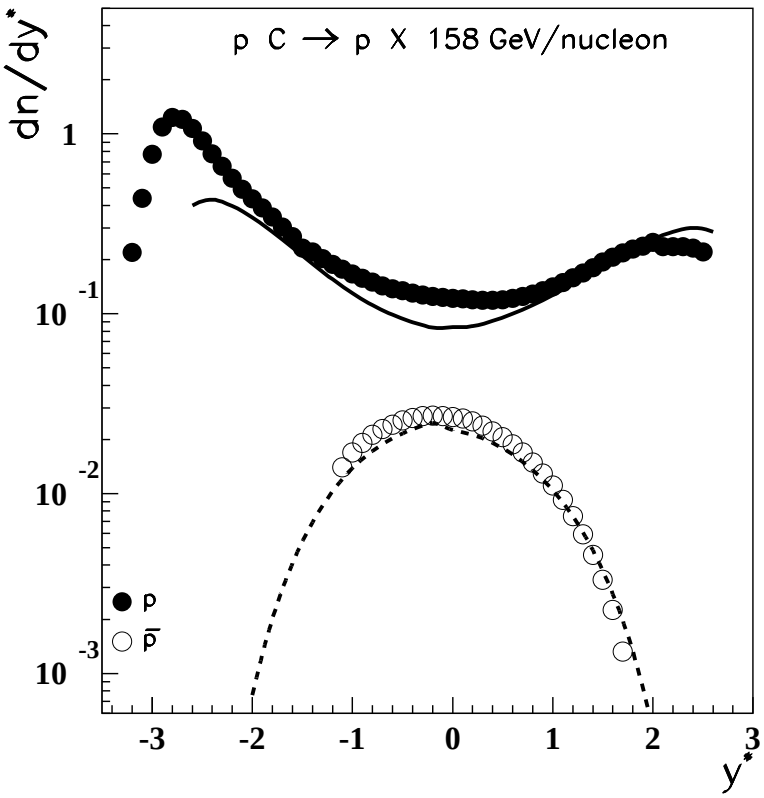

Figure 11: The rapidity dependence of the production denstities of p and $\overline{p}$ baryons produced in pC collisions measured by the NA49 Collaboration at 158 GeV/c [72], together with the results of the QGSM calculations. The theoretical curves correspond to those in Fig 4.

energies, up to λ_s=0.32 at LHC energies. In the present paper we do not present any parametrisation of the energy dependence of the value of the parameter $\lambda_s(E)$, since amount of experimental data is not enough yet to check up this behaviour.

Acknowledgements We thank N. Armesto and C. Pajares for useful discussions. We also are grateful to N.I. Novikova for technical help.

This paper was supported by Ministerio de Economía y Competitividad of Spain (FPA2014−58293), the Spanish Consolider-Ingenio 2010 Programme CPAN (CSD2007-00042), by Xunta de Galicia, Spain (2011/PC043), and, in part, by Russian grant RSGSS-3628.2008.2 and by State Committee of Science of the Republic of Armenia, Grant-13-1C023.-00281.

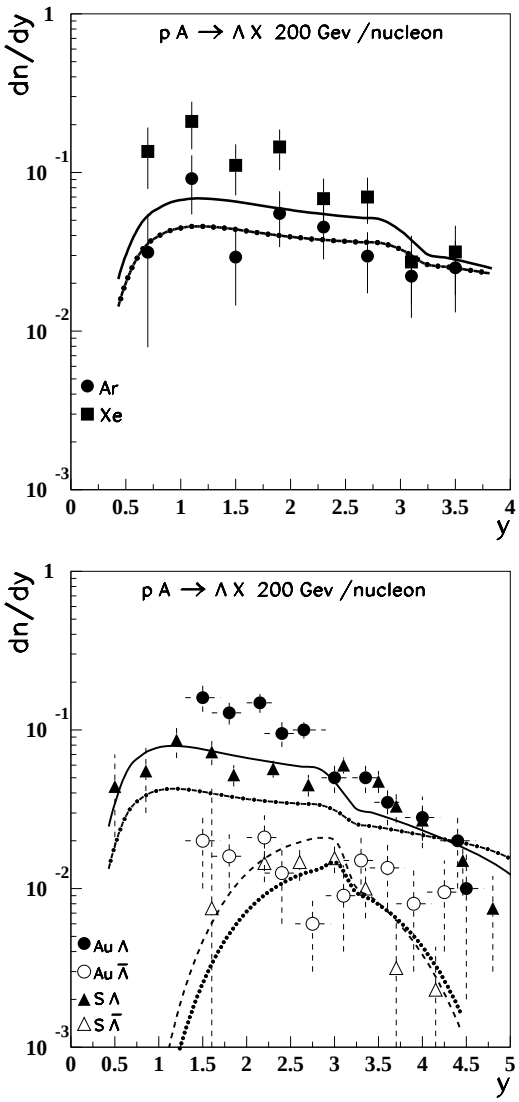

Figure 12: The experimental data on the rapidity dependence of the production denstities of Λ hyperon produced in proton collisions on Ar and Xe nuclei [73] (upper panel) and of Λ and $\overline{\Lambda}$ hyperons produced in proton collisions on S and Au nuclei [74, 75, 76] (lower panel), all at 200 GeV/c, together with the results of the corresponding QGSM calculations (see the main text por the description of the different curves).

References

[1] T. Sjöstrand, P.Scands, Eur. Phys. J. **C39**, 129 (2005).

[2] P. Scands, Phys. Rev. **D82**, 074018 (2010).

[3] W.-T. Deng, X.-N. Wang, and R. Xu, Phys. Rev. **C53**, 014915 (2011).

[4] A.B. Kaidalov and K.A. Ter-Martirosyan, Yad. Fiz. **39**, 1545 (1984); **40**, 211 (1984).

[5] A.B. Kaidalov, Sov. J. Nucl. Phys. **66**, 1994 (2003); Yad. Fiz. **66**, 2014 (2003).

[6] A.B. Kaidalov and O.I. Piskounova, Yad. Fiz. **41**, 1278 (1985); Z. Phys. **C30**, 145 (1986).

[7] Yu.M. Shabelski, Yad. Fiz. **44**, 186 (1986).

[8] G.H. Arakelyan, C. Merino, C. Pajares, and Yu.M. Shabelski, Eur. Phys. J. **C54**, 577 (2008) and hep-ph/0709.3174.

[9] C. Merino, C. Pajares, and Yu.M. Shabelski, Eur. Phys. J. **C71**, 1652 (2011).

[10] G.H. Arakelyan, A. Capella, A.B. Kaidalov, and Yu.M. Shabelski, Eur. Phys. J. **C26**, 81 (2002) and hep-ph/0103337.

[11] A.B. Kaidalov, K.A. Ter-Martirosyan, and Yu.M. Shabelski, Yad. Fiz. **43**, 1282 (1986).

[12] Yu.M. Shabelski, Z. Phys. **C38**, 569 (1988).

[13] G.H. Arakelyan, A.B. Kaidalov, C. Merino, and Yu.M. Shabelski, Phys. Atom. Nucl. **74**, 126 (2011) and arXiv:1004.4074[hep-ph].

[14] C. Merino, C. Pajares, and Yu.M. Shabelski, Eur. Phys. J. **C73** (2013) 1, 2266 and arXiv:1207.6900[hep-ph].

[15] G.H. Arakelyan, C. Merino, C. Pajares, and Yu.M. Shabelski, Phys. Atom. Nucl. **76**, 316 (2013) and arXiv:1207.6899[hep-ph].

[16] V.A. Abramovsky, V.N. Gribov, and O.V. Kancheli, Yad. Fiz. **18**, 595 (1973).

[17] A.B. Kaidalov, Sov. J. Nucl. Phys. **45**, 902 (1987); Yad. Fiz. **43**, 1282 (1986).

[18] V.V. Anisovich and V.M. Shekhter, Nucl. Phys. B**55**, 455 (1973).

[19] A. Capella and C.A. Salgado, Phys. Rev. **C60**, 054906 (1999).

[20] O.I. Piskounova, arXiv:1405.4398[hep-ph].

[21] O.I. Piskounova, Phys. Atom. Nucl. **70**, 1110 (2007) and hep-ph/0604157.

[22] C. Merino, C. Pajares, and Yu.M. Shabelski, Eur. Phys. J. **C59**, 691 (2009) and arXiv:0802.2195 [hep-ph].

[23] C. Merino, M.M. Ryzhinski, and Yu.M. Shabelski, Eur. Phys. J. **C62**, 491 (2009); Lecture given by Yu.M. Shabelski at The XLIII PNPI Winter School on Physics, St.Petersburg (Russia), February 2009, arXiv:0906.2659[hep-ph].

[24] X. Artru, Nucl. Phys. **B85**, 442 (1975).

[25] M. Imachi, S. Otsuki, and F. Toyoda, Prog. Theor. Phys. **52**, 346 (1974); **54**, 280 (1976); **55**, 551 (1976).

[26] G.C. Rossi and G. Veneziano, Nucl. Phys. **B123**, 507 (1977).

[27] D. Kharzeev, Phys. Lett. **B378**, 238 (1996).

[28] A. Capella, A. Kaidalov, and J. Tran Thanh Van, Heavy Ion Phys. **9**, 169 (1999).

[29] F. Bopp and Yu.M. Shabelski, Yad. Fiz. **68**, 2155 (2005) and hep-ph/0406158; Eur. Phys. J. **A28**, 237 (2006) and hep-ph/0603193.

[30] K. Aamodt *et al.*, ALICE Collaboration, Phys. Rev. Lett. **601** 5, 072002 (2010) and arXiv:1006.5432[hep-ex].

[31] Yu.M. Shabelski, Yad. Fiz. **26**, 1084 (1977); Nucl. Phys. **B132**, 491 (1978).

[32] L. Bertocchi and D. Treleani, J. Phys. **G3**, 147 (1977).

[33] J. Weis, Acta Phys. Polonica **B7**, 85 (1977).

[34] T. Jaroszewicz *et al.*, Z. Phys. **C1**, 181 (1979).

[35] Yu.M. Shabelski, Sov. J. Nucl. Phys. **45**, 143 (1987); Z. Phys. **C38**, 569 (1988).

[36] B.B. Back *et al.*, PHOBOS Collaboration, Phys. Rev. Lett. **85**, 3100 (2000).

[37] K. Adcox *et al.*, PHENIX Collaboration, Phys. Rev. Lett. **86**, 500 (2001).

[38] A. Capella, C. Merino, and J. Tran Thanh Van, Phys. Lett. **B265** 415 (1991).

[39] Yu.M. Shabelski, Z. Phys. **C57**, 409 (1993).

[40] O.V. Kancheli, JETP Lett. **18**, 274 (1973).

[41] G.V. Davidenko and N.N. Nikolaev, Yad. Fiz. **24**, 772 (1976).

[42] A. Schwimmer, Nucl. Phys. **B94**, 445 (1975).

[43] J. Dias de Deus, R. Ugoccioni, and A. Rodrigues, Phys. Lett. **B458**, 402 (1999).

[44] J. Dias de Deus, R. Ugoccioni, and A. Rodrigues, Eur. Phys. J. **C16**, 537 (2000).

[45] M.A. Braun and C. Pajares, Phys. Rev. Lett. **85**, 4864 (2000).

[46] J. Dias de Deus and Yu.M. Shabelski, Eur. Phys. J. **A20**, 457 (2004).

[47] P. Brogueira, J. Dias de Deus, and C. Pajares, Phys. Rev. **C75**, 054908 (2007).

[48] C. Merino, C. Pajares, and J. Ranft, Phys. Lett. **B276**, 168 (1992).

[49] H.J. Möhring, J. Ranft, C. Merino, and C. Pajares, Phys. Rev. **D47**, 4142 (1993).

[50] N.S. Amelin, M.A. Braun, and C. Pajares, Z. Phys. **C63**, 507 (1994).

[51] J. Dias de Deus and C. Pajares, Phys. Lett. **B695**, 211 (2012) and arXiv:1011.1099[hep-ph].

[52] G. Aad *et al.*, ATLAS Collaboration, Phys. Rev. **D85**, 012001 (2012).

[53] V. Khachatryan *et al.*, CMS Collaboration, JHEP 1105 (2011) 064.

[54] D. Barna, NA49 Collaboration, PhD Thesis, 2002.

[55] J.W. Chapman *et al.*, Phys. Lett **B47**, 465 (1975).

[56] D. Brick *et al.*, Nucl. Phys. **B164**, 1 (1980).

[57] F. Lopinto *et al.*, Phys. Rev. **D22**, 323 (1980).

[58] K. Jaeger *et al.*, Phys. Rev. **D11**, 2405 (1975).

[59] A. Sheng *et al.*, Phys. Rev. **D11**, 722 (1975).

[60] H. Kichimi *et al.*, Phys. Rev. **D20**, 37 (1979).

[61] B. Abelev *et al.*, STAR Collaboration, Phys. Rev. **C75**, 064901 (2007).

[62] M. Aguilar-Benitez *et al.*, Z. Phys. **C50**i, 405 (1991).

[63] A. Adare *et al.*, PHENIX Collaboration, Phys. Rev. **C83**, 064903 (2011).

[64] B. Abelev *et al.*, STAR Collaboration, Phys. Rev. **C79**, 034909 (2009).
[65] S. Chatrchyan *et al.*, CMS Collaboration, Eur. Phys. J. **C72**, 2164 (2012).
[66] K. Aamodt *et al.*, ALICE Collaboration, Eur. Phys. J. **C71**, 1655 (2011).
[67] J.K. Adam *et al.*, ALICE Collaboration, Eur. Phys. J. **C75**, 226 (2015).
[68] T. Anticic *et al.*, NA49 Collaboration, Eur. Phys. J. **C65**, 9 (2010).
[69] B. Abelev *et al.*, Phys. Lett. **B712**, 309 (2012).
[70] S. Chatrchyan *et al.*, CMS Collaboration, Eur. Phys. J. **C74**, 2847 (2014).
[71] F. Antinori *et al.*, NA57 Collaboration, J. Phys. **G32**,427 (2006).
[72] B. Baatar *et al.*, NA49 Collaboration, Eur. Phys. J. **C73**, 2364 (2013).
[73] E. Derado *et al.*, NA5 Collaboration, Z. Phys. **C50**, 31 (1991).
[74] A. Bamberger *et al.*, NA35 Collaboration, Z. Phys. **C41**, 25 (1989).
[75] J. Bartke *et al.*, NA35 Collaboration, Z. Phys. **C48**, 191 (1990).
[76] T. Alber *et al.*, NA35 Collaboration, Z. Phys. **C64**, 195 (1994).